

Cite this: *Chem. Sci.*, 2021, 12, 8477

All publication charges for this article have been paid for by the Royal Society of Chemistry

The key role of the latent N–H group in Milstein's catalyst for ester hydrogenation†

John Pham, Cole E. Jarczyk, Eamon F. Reynolds, Sophie. E. Kelly, Thao Kim, Tianyi He, Jason M. Keith* and Anthony R. Chianese*

We previously demonstrated that Milstein's seminal diethylamino-substituted PNN-pincer–ruthenium catalyst for ester hydrogenation is activated by dehydroalkylation of the pincer ligand, releasing ethane and eventually forming an NHEt-substituted derivative that we proposed is the active catalyst. In this paper, we present a computational and experimental mechanistic study supporting this hypothesis. Our DFT analysis shows that the minimum-energy pathways for hydrogen activation, ester hydrogenolysis, and aldehyde hydrogenation rely on the key involvement of the nascent N–H group. We have isolated and crystallographically characterized two catalytic intermediates, a ruthenium dihydride and a ruthenium hydridoalkoxide, the latter of which is the catalyst resting state. A detailed kinetic study shows that catalytic ester hydrogenation is first-order in ruthenium and hydrogen, shows saturation behavior in ester, and is inhibited by the product alcohol. A global fit of the kinetic data to a simplified model incorporating the hydridoalkoxide and dihydride intermediates and three kinetically relevant transition states showed excellent agreement with the results from DFT.

Received 3rd February 2021
Accepted 14th May 2021

DOI: 10.1039/d1sc00703c

rsc.li/chemical-science

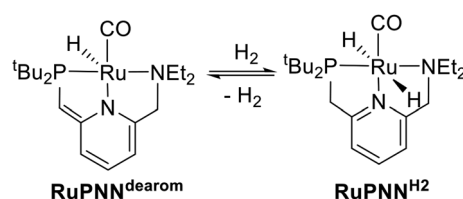
Introduction

Catalytic transformations relying on metal–ligand-cooperative hydrogenation or dehydrogenation of polar substrates have seen a dramatic expansion in development over the past decade and a half, following the disclosure by Milstein and co-workers of the PNN-pincer–ruthenium complex **RuPNN^{dearom}** (Scheme 1), shown to be active under relatively mild conditions for the hydrogenation of esters to alcohols,¹ as well as the reverse reaction, the acceptorless dehydrogenative coupling (ADC) of primary alcohols to esters.² This complex has since been applied to a wide range of mechanistically related transformations.³ In the original reports, the dearomatized complex **RuPNN^{dearom}** was shown to react reversibly with hydrogen at room temperature to give the rearomatized dihydride complex **RuPNN^{H2}**. Based on this observation, a mechanism was proposed that involved this heterolytic cleavage of hydrogen as a key step in catalytic ester hydrogenation.

In the years since the initial reports on **RuPNN^{dearom}**, many researchers have studied the effect of catalyst structure on activity in ester hydrogenation, and several highly optimized catalysts have been discovered that give more than 10 000 turnovers at full substrate conversion.⁴ Common to almost all of these elite catalysts is an N–H functional group on the ligand. In some cases, the N–H group was demonstrated to be essential for high catalytic activity through the synthesis of control ligands where N–H was replaced with N–Me, N–Bn, or O.^{4a,c,e} In many cases, minimum-energy pathways involving deprotonation of the N–H group have been identified through density functional theory,^{4c,f,h,i,5} although recent computational work has suggested that in some cases, the N–H group may function in catalysis as a hydrogen-bond donor without being deprotonated on the catalytic cycle.^{5b,6} Although many of the most highly active catalysts for ester hydrogenation feature an N–H functional group, several structural motifs lacking an N–H group have also been reported. In particular, several ruthenium catalyst variants

Department of Chemistry, Colgate University, 13 Oak Drive, Hamilton, New York 13346, USA. E-mail: jkeith@colgate.edu; achianese@colgate.edu

† Electronic supplementary information (ESI) available: Computational and experimental methods. Alternative pathways calculated by DFT and table of computed energies, images of NMR spectra for **RuPNN^{HOEt}**, details of kinetic modeling (PDF). Atomic coordinates (XYZ) for all computed molecular structures, compiled as one file readable by the free program Mercury³² (compiled.xyz). Animations (GIF) for the imaginary vibrational modes of all calculated transition states (TS animations.zip). Copasi model (model.cps) and kinetic data in the format accepted by Copasi (data.txt). CCDC 2057608 and 2057609. For ESI and crystallographic data in CIF or other electronic format see DOI: 10.1039/d1sc00703c



Scheme 1 Reversible activation of hydrogen mediated by **RuPNN^{dearom}**.

featuring dialkylamino side groups like **RuPNN^{dearom}** have shown activity.^{4d,7}

During mechanistic studies of our previously reported^{7c,d,8} CNN-pincer-ruthenium catalysts for ester hydrogenation, we made a surprising observation: precatalysts featuring NEt_2 or N^iPr_2 side groups underwent an unexpected dehydroalkylation reaction, releasing an equivalent of ethane or propane early on in catalytic reactions.⁹ The observation of catalytic induction periods concomitant with the release of alkane established that dehydroalkylation was a necessary step in formation of the active catalyst. Milstein's catalyst **RuPNN^{dearom}**, which features an NEt_2 side group, also showed an induction period for ester hydrogenation, and released ethane concomitantly with the onset of catalytic activity. By heating our CNN- and Milstein's PNN-pincer precatalysts in the presence of tricyclohexylphosphine, we were able to trap the products of dehydroalkylation as five-coordinate ruthenium(0) complexes, where the dialkylamino side group was transformed to an imine functionality (PNN variant shown in Scheme 2). **RuPNN^{imine}**, the ruthenium(0) derivative of **RuPNN^{dearom}**, is dramatically more active as a precatalyst for ester hydrogenation than its precursor, and is by some measures the most efficient catalyst currently known for ester hydrogenation, giving in excess of 10 000 catalytic turnovers at room temperature with no added base. Several catalysts have been reported to operate at^{4d,10} or near^{4b,c,5a,11} room temperature, but require significant quantities of strongly basic additives such as NaO^tBu and KO^tBu . Conversely, several catalysts operate without the need for added base, but require temperatures of 80 °C or higher.^{1,5g,12}

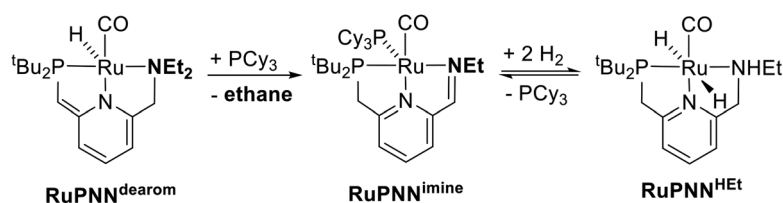
To further probe the catalyst speciation under operating conditions, we monitored the reaction of **RuPNN^{imine}** with hydrogen at room temperature. Under 10 bar H_2 , **RuPNN^{imine}** converts quantitatively to the dihydride complex **RuPNN^{HEt}**, involving a net hydrogenation of the imine functional group and a net oxidative addition of H_2 to the ruthenium center (Scheme 2). As **RuPNN^{HEt}** contains a ruthenium hydride and N–H group, we proposed⁹ that it may be an active catalytic intermediate in reactions initiated by **RuPNN^{imine}** and **RuPNN^{dearom}**, operating by a metal–ligand-cooperative mechanism analogous to that proposed for other elite N–H-containing catalysts.

The discovery of the dehydroalkylative activation of **RuPNN^{dearom}** has potentially broad mechanistic implications. Because we have demonstrated that **RuPNN^{dearom}** is not a kinetically competent intermediate and must undergo dehydroalkylation prior to being catalytically active for ester hydrogenation, it is unlikely that the originally proposed mechanism¹ is correct. Three reports in the literature apply density

functional theory to predict the mechanism of ester hydrogenation or the reverse ADC, catalyzed by **RuPNN^{dearom}**.¹³ Since these studies rely on the catalytic intermediacy of **RuPNN^{dearom}** or **RuPNN^{H2}**, they too are unlikely to be correct. More broadly, **RuPNN^{dearom}** has been applied as a catalyst for a wide range of related hydrogenation and dehydrogenation reactions, including amine–alcohol coupling,^{3a–d} couplings of amines^{3e} or alcohols^{3f} with esters, organic carbonate hydrogenation,^{3g} carbon dioxide hydrogenation,^{3h} and amide α -alkylation with alcohols.³ⁱ All of these transformations are conducted at or above 100 °C, where the dehydroalkylation reaction occurs rapidly ($t_{1/2} = 6$ min at 100 °C). As such, it is possible that **RuPNN^{dearom}** is inactive prior to dehydroalkylation in these systems as well, which may call into question the DFT studies of these transformations.^{13a,14}

Kinetic studies have the potential to validate or falsify the findings from computation, as they show conclusively what species are consumed or released on the pathway from the turnover-frequency-determining intermediate (TDI) to the turnover-frequency-determining-transition state (TDTS).¹⁵ For example, recent kinetic investigations of metal-catalyzed hydroformylation¹⁶ and ketone hydrogenation¹⁷ have provided deep insight into the underlying reaction mechanisms. Although catalytic ester hydrogenation and its microscopic reverse, ADC, have been studied intensively through computational methods, detailed experimental mechanistic investigations, especially kinetic studies, are scarce. In studies of an iridium–bipyridine catalyst system, Brewster, Sanford, and Goldberg determined the dependence of turnover number at low conversion on the concentrations of catalyst, hydrogen, and ester.^{12h} However, as reactions were not monitored over time, this study did not probe for potential activation of catalyst observed as an induction period, and did not probe for potential product inhibition. Filonenko, Pidko and coworkers reported time-course studies of ester hydrogenation catalyzed by CNC-pincer-ruthenium complexes, but did not determine the detailed dependences of the rate on concentrations.^{4e} O and Morris also reported time-course studies for ester hydrogenation catalyzed by ruthenium complexes of NHC–amine ligands, but also did not determine a rate law.^{5a}

In this paper, we describe a computational and experimental mechanistic study of ester hydrogenation catalyzed by **RuPNN^{imine}**. We report the crystallographic characterization of the key dihydride intermediate **RuPNN^{HEt}**, and the synthesis and characterization of the ruthenium-hydrido-alkoxide **RuPNN^{HOEt}**, which represents the catalytic resting state and TDI. Detailed kinetic studies show an induction period at room



Scheme 2 Dehydroalkylation of Milstein's catalyst and reversible H_2 addition giving **RuPNN^{HEt}**.



temperature during which $\text{RuPNN}^{\text{imine}}$ is converted to the active form, and after which the reaction shows first-order dependence on [catalyst] and [hydrogen], first-order saturation behavior in [ester], and a transition from inverse second-order to inverse-first-order inhibition by the product alcohol. All of this kinetic behavior, as well as the overall rate of reaction, is consistent with the minimum-energy pathway calculated using density functional theory.

Computational mechanistic analysis

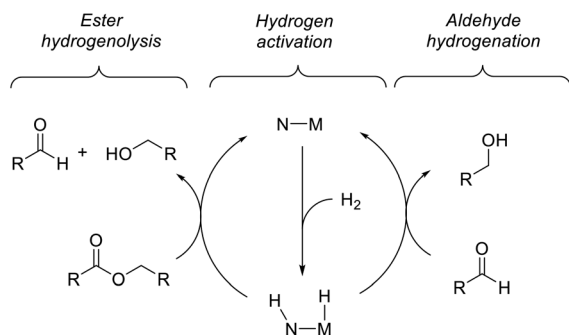
Background

Previous computational studies of the mechanism of ester hydrogenation catalyzed by transition-metal complexes with a pendant N-H functional group have converged on a bicyclic pathway,^{4c,f,h,i,5} which can be separated into three linear sequences (Scheme 3). In the hydrogen-activation sequence, the H-H bond is cleaved heterolytically, placing a hydride on the metal center and a proton on the basic nitrogen center. In ester hydrogenolysis, these hydrogen atoms are transferred to the ester substrate, and cleavage of the C-O bond facilitated by the catalyst produces an aldehyde intermediate and one product alcohol molecule. In the aldehyde-hydrogenation sequence, the intermediate aldehyde is reduced to alcohol by the hydrogenated form of the catalyst. In one important variation on this scheme, it is possible that the nitrogen remains protonated throughout catalysis if an exogenous alkoxide base participates in hydrogen cleavage directly.^{5b,6}

We chose ethyl acetate as an appropriate model ester for computational study, for several reasons: (1) its use is well-precedented in both experimental and computational work; (2) it is small enough to minimize issues resulting from a large number of potential conformations; (3) it is large enough to appropriately model the steric interactions of common ester substrates with the catalyst. In particular, we expected the energetics of ethyl acetate hydrogenation to closely mimic those of hexyl hexanoate, which we employed in the kinetic studies described below.

Consideration of plausible resting states

We began our study by comparing the relative free energies of plausible catalyst resting states, in each case considering the

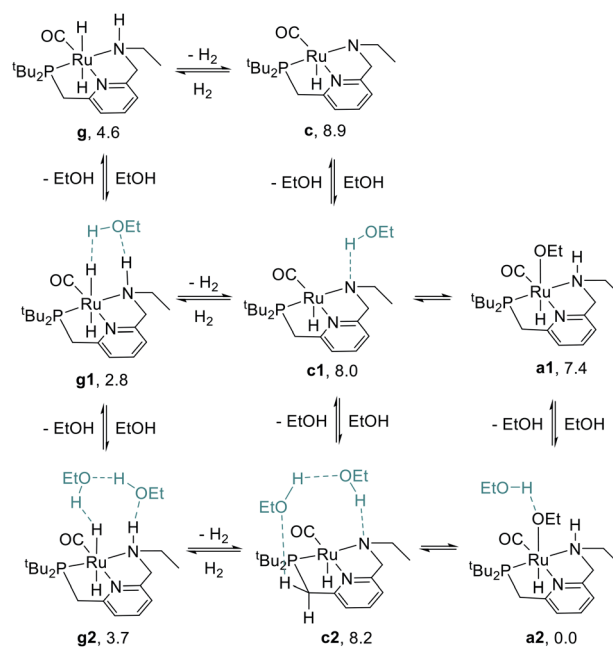


Scheme 3 Two linked catalytic cycles for ester hydrogenation.

effect of hydrogen-bonded product ethanol molecules (Scheme 4). Dihydride species **g**, **g1**, and **g2** were identified, and we found a small ($<2.0 \text{ kcal mol}^{-1}$) effect of binding to ethanol on the standard-state free energy. The calculated structure of **g** very closely matches the crystal structure of $\text{RuPNN}^{\text{HEt}}$, described below. We found that unsaturated intermediates **c**, **c1**, and **c2**, related to the dihydride compounds by formal loss of H_2 , were approximately $4\text{--}5 \text{ kcal mol}^{-1}$ higher in energy than their dihydride counterparts. We also considered hydridoalkoxide species **a1** and **a2**. Although the “free” species **a1** is similar in energy to its unsaturated counterpart **c1**, the hydridoalkoxide **a2** with an additional hydrogen-bonded ethanol molecule is much more stable than **c2**, and is identified as the catalyst resting state. As described below, the calculated structure of **a2** closely matches the crystal structure of $\text{RuPNN}^{\text{HOEt}}$, and the experimental kinetics are consistent with **a2** as the catalyst resting state.

Pathway for hydrogen activation

We began by probing a range of possible pathways for the activation of H_2 , informed by the rich history of prior work on related reactions. Our search for the MEP for H_2 activation covered metal-ligand-cooperative heterolytic cleavage involving the N-H functional group, as proposed by Noyori and co-workers for their seminal carbonyl hydrogenation catalysts,¹⁸ both with and without explicit ethanol molecules to serve as proton shuttles. Noyori-type mechanisms for H_2 activation have been identified for a range of catalysts for ester hydrogenation or ADC.^{4c,f,h,i,5a,c-j,6d} We also carefully searched for pathways involving cooperative activation of H_2 through the ruthenium center and an ethoxide anion, which Dub *et al.* showed can



Scheme 4 Species considered as plausible resting states. Energies given represent standard-state free energies in kcal mol^{-1} at 298.15 K relative to **a2**.



bypass the deprotonation of the N–H group on the pincer ligand.^{5b,6} Lastly, we exhaustively examined pathways for H₂ activation involving deprotonated CH₂ linkers on the pincer ligand, as originally proposed by Milstein and coworkers,¹ and identified by DFT in many studies.^{13a,14a–e,g,19}

Fig. 1 shows the pathway we identified with the lowest overall barrier, which we describe as a “proton brigade” because of the involvement of two ethanol molecules in the stepwise cleavage of the H–H bond. Beginning with the resting state **a2**, whose experimental characterization is described in the next section, a double proton transfer through **a2-b2-TS** (ref. 20) gives the N-deprotonated species **b2** with a neutral ethanol molecule coordinated to Ru. Then, this ethanol dissociates to give the unsaturated species **c2**, which transfers a proton back to nitrogen to give **d2** before binding H₂ in the σ -complex **f2**, in which the nitrogen is protonated and an ethoxide anion is stabilized by two hydrogen bonds. Then, H₂ is cleaved through the proton-shuttle transition state **f2-g2-TS**, resulting in the dihydride species **g2** (with two associated ethanol molecules) or **g1** (with one associated ethanol). Although this pathway does involve temporary deprotonation of nitrogen between **a2** and **d2**, the reformation of the N–H bond is not concerted with H₂ cleavage. We also located a pathway connecting **a2** to **d2** where the N–H bond remains intact (Fig. S1†), and a pathway connecting **c2** to **f2** where hydrogen coordination occurs before proton transfer to nitrogen (Fig. S2†), both with slightly higher barriers.

The MEP identified for hydrogen activation requires passing through **f2-g2-TS** at 15.0 kcal mol^{−1}. Notably, this proton-brigade pathway relies on the inclusion of two explicit ethanol

molecules, both for the low overall barrier and for the stepwise proton-shuttle mechanisms. For comparison, we calculated analogous pathways involving only one ethanol molecule as proton shuttle and involving no ethanol molecules. These pathways, both concerted, are described in detail in the ESI (Fig. S3†), and were found to proceed through higher overall barriers of 18.6 and 25.3 kcal mol^{−1}, respectively.

We also searched exhaustively for pathways involving the activation of H₂ mediated by deprotonated CH₂ linkers of the pincer ligand, both with and without explicit ethanol molecules as proton shuttles. These pathways, described in detail in the ESI,† would implicate dearomatized species similar to **RuPNN^{dearom}** as key intermediates in catalysis. All mechanisms of this nature were found to proceed through higher barriers for H₂ cleavage, with a lowest identified barrier of 25.6 kcal mol^{−1} for mechanisms involving the NCH₂ linker and 23.7 kcal mol^{−1} for the PCH₂ linker. In summary, our work shows that the presence of the N–H functional group is essential for activation of hydrogen with a low barrier. The N–H group is temporarily deprotonated in our MEP, but a pathway where the N–H group remains protonated and instead serves to stabilize intermediates and transition states through hydrogen bonding is energetically similar, and cannot be excluded by DFT. Pathways involving deprotonation of CH₂ linkers have significantly higher barriers and can be excluded.

Pathway for ester hydrogenolysis

The ester hydrogenolysis portion of the catalytic cycle involves the hydrogenation of the carbonyl functional group and cleavage of the C–O bond, ultimately releasing one product

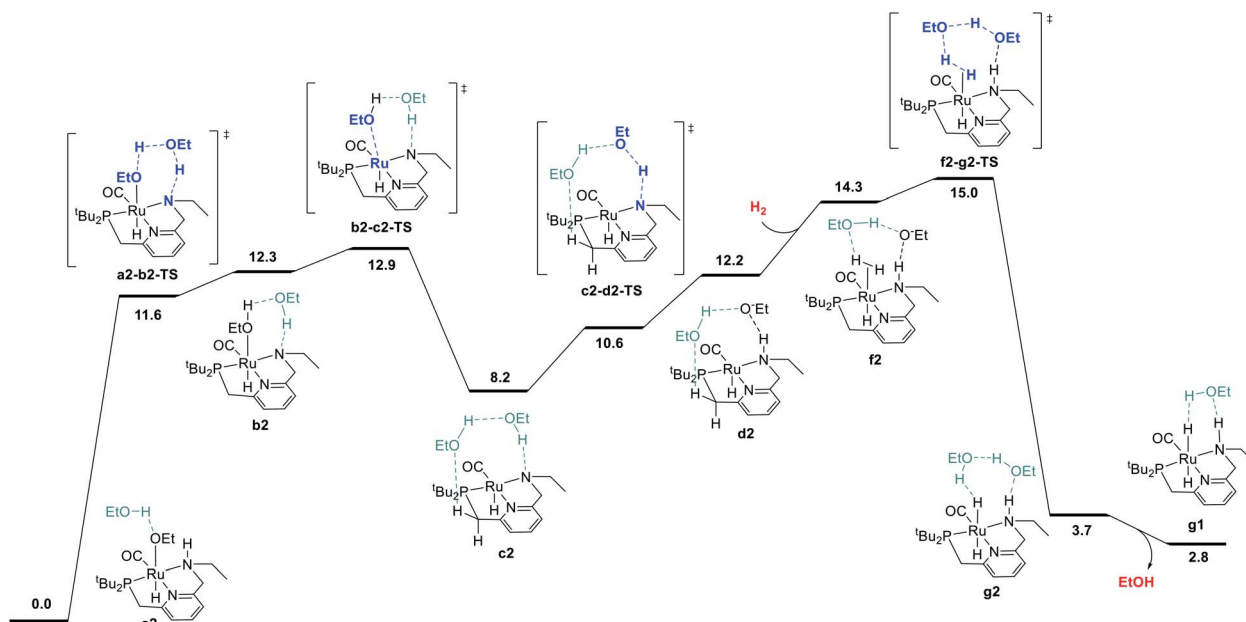


Fig. 1 Minimum-energy pathway for hydrogen activation to convert the hydrido-ethoxide resting state **a2** into dihydride intermediate **g1**. Throughout this work, atoms in bold and blue represent those atoms principally involved in bond-breaking and bond-forming events in transition states. Atoms shown in turquoise represent neutral ethanol molecules interacting with the main fragment through hydrogen bonds. Small molecules entering or leaving the sequence are in red. Energies given represent standard-state free energies in kcal mol^{−1} at 298.15 K, relative to **a2** and the organic reactants unless otherwise stated.

alcohol molecule and an aldehyde intermediate. Prior work on many systems has identified the transfer of hydride from the metal to the carbonyl carbon as a key initial step, which generates a hemiacetaloxide intermediate. Two principal pathways for cleavage of the C–OEt bond have emerged, which have been shown to have similar barriers for related catalysts. These pathways differ by the coordination of either the aldehyde oxygen^{4c,f,i,5d,f,h,6d} or the alkoxide oxygen^{4h,5a,h,i,6d,21} to Ru during C–O cleavage. In our system, we find these mechanisms to have nearly identical barriers, as described below. The pathway shown in Fig. 4 is an example of the former mechanism. Beginning from the dihydride intermediate **g1**, the ester replaces the hydrogen-bonded alcohol molecule to give the reactant complex **h**, which transfers hydride from Ru to C to give the C–H σ -complex **i**, where the hemiacetaloxide oxygen is stabilized by hydrogen-bonding to the N–H. Then, proton transfer from N to O gives **j**,²⁰ which rearranges to place the hydroxyl oxygen on Ru in **k**, followed by reprotonation of nitrogen and subsequent hydrogen bond formation to give the Ru-bound hemiacetaloxide complex **m**. Then, cleavage of the C–O bond, concerted with proton transfer from N back to O, gives **n**, a loosely-bound complex of the product ethanol and intermediate acetaldehyde. Replacement of the aldehyde with another ethanol molecule gives **c2**, which connects back to the hydrogen activation pathway in Fig. 1 and completes the first hydrogenation cycle.

The ester hydrogenolysis pathway shown above proceeds through a highest barrier of 17.4 kcal mol^{−1}, which is the free energy of the intermediate species **n**. Notably, intermediates **k** and **n** and transition states **k-l-TS** and **m-n-TS** all have essentially identical free energies of 17.0–17.4 kcal mol^{−1}. Thus, flux

through this sequence is limited by both the cleavage of the O–H bond in **k** (essentially barrierless in the forward direction) and the cleavage of the C–O bond in **m** (essentially barrierless in the reverse direction).²⁰

We also identified a different pathway for C–O cleavage, with a nearly identical overall barrier of 18.1 kcal mol^{−1}, which directly places the newly formed ethoxide rather than the aldehyde on ruthenium (Fig. S8†). Similar to the transformation identified by Hasanayn and termed a hydride-alkoxide metathesis,²¹ this pathway would predict identical kinetic behavior as the one shown below in Fig. 2. In the process of establishing the twin minimum-energy pathways described in Fig. 2 and S8,† we characterized diastereomeric sequences where the ester initially coordinates to Ru through the opposite face, and pathways involving an explicit ethanol molecule. As described in detail in the ESI,† we found slightly higher overall barriers for the diastereomeric pathways (Fig. S10 and S12†) and similar overall barriers for pathways involving an explicit ethanol molecule (Fig. S11 and S14†). We also calculated a ruthenium-free pathway for the conversion of the hemiacetal to ethanol and acetaldehyde (Fig. S15†), and find a much higher barrier of 36.4 kcal mol^{−1}, in line with previous work.^{6d,14h} In summary, we find that ester hydrogenolysis proceeds in our system by well-precedented mechanisms for ruthenium–pincer catalysts possessing an N–H group, and that the decomposition of the hemiacetal is mediated by the ruthenium–pincer catalyst.

Pathway for aldehyde hydrogenation

The final portion of the catalytic cycle involves hydrogenation of the aldehyde intermediate to give the second equivalent of alcohol product. This sequence, as mediated by a ruthenium

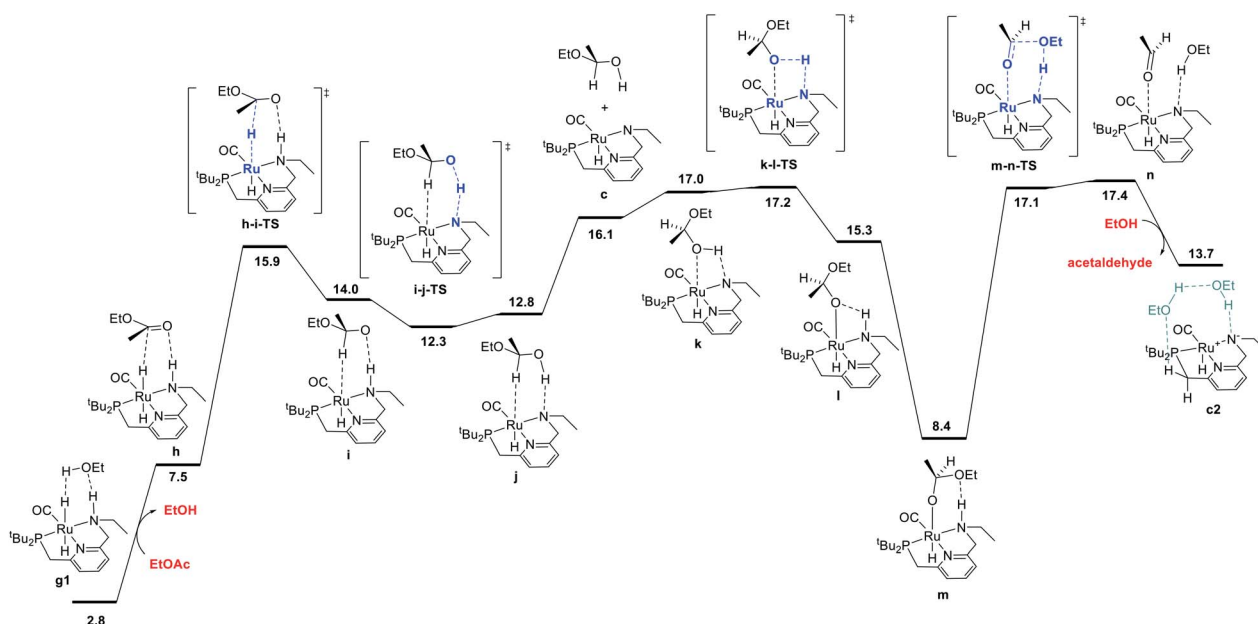


Fig. 2 MEP for hydrogenolysis of ethyl acetate to acetaldehyde and ethanol, accompanied by conversion of dihydride intermediate **g1** into unsaturated intermediate **c2**, which connects back to the hydrogen-activation pathway shown in Fig. 1. Note that the standard-state free energy of 13.7 kcal mol^{−1} reported here for **c2** corresponds to release of acetaldehyde and binding of ethanol from **n**, whereas the free-energy of 8.2 kcal mol^{−1} reported for **c2** in Fig. 1 is calculated against the ethyl acetate and dihydrogen reactants.

hydride complex with a pendent N–H functional group on the ligand, has been studied extensively through DFT in the context of ester hydrogenation, but also has a longer history dating back to the original Noyori catalysts, which were highly efficient for aldehyde and ketone hydrogenation.¹⁸ For ester hydrogenation catalysts, the aldehyde hydrogenation step is generally found to have a lower barrier than the ester hydrogenolysis step, which along with the thermodynamic instability of the aldehyde with respect to reactants, is consistent with the lack of buildup of aldehyde in catalytic reactions. For our catalytic system, we identified the pathway shown in Fig. 3, beginning with coordination of the aldehyde to form **r**. This is followed by stepwise transfer of hydride and proton to the substrate from the ruthenium and nitrogen centers, respectively, giving intermediates **s** and **t**. Dissociation of the C–H σ -complex gives **c1**, which connects back to the hydrogen activation pathway.

In some recent studies,^{6,13c,22} proton transfer from the ligand to the alkoxide oxygen was calculated to have a higher barrier than proton transfer from an exogenous alcohol molecule, which enables the construction of a pathway for hydrogenation where the ligand N–H group (or CH₂ linker) is never deprotonated. Pathways like this may have been missed in earlier work because of the optimization of structures without a solvent model, which can favor concerted proton/hydride transfer pathways and disfavor ion-pair intermediates such as **s**. In our work, conducting geometry optimizations using a toluene continuum solvent model allowed the identification of the

intermediate **s**. As proton transfer from N to O through **s-t-TS** is barrierless²⁰ and strongly exergonic in our system, we did not search extensively for additional pathways for conversion of the aldehyde to ethanol.

Summary and predicted kinetics

In summary, we have identified MEPs for hydrogen activation, ester hydrogenolysis, and aldehyde hydrogenation in ester hydrogenation catalyzed by **RuPNN^{HEt}**, which forms *in situ* from **RuPNN^{imine}** as we have shown experimentally.⁹ Fig. 4 shows a simplified energy diagram depicting key intermediates and transition states relevant in predicting the kinetics of hydrogenation through the energetic span model.¹⁵ The hydrido-alkoxide complex **a2** is predicted to be the turnover-frequency-determining intermediate (TDI). The highest-energy transition states in the hydrogen activation and ester hydrogenolysis sequences are **f2-g2-TS** and **m-n-TS**, respectively. Although intermediate **n** is calculated to be higher than **m-n-TS** by 0.3 kcal mol^{−1},²⁰ we have used **m-n-TS** in our kinetic analysis for consistent application of transition-state theory to calculate rate constants. The 2.1 kcal mol^{−1} free-energy difference between **f2-g2-TS** and **m-n-TS** is likely within the error of the DFT method, especially considering the changes in molecularity involved: between **a2** and **f2-g2-TS**, a hydrogen molecule is consumed, and between **f2-g2-TS** and **m-n-TS**, two ethanol molecules are released and ethyl acetate is consumed.

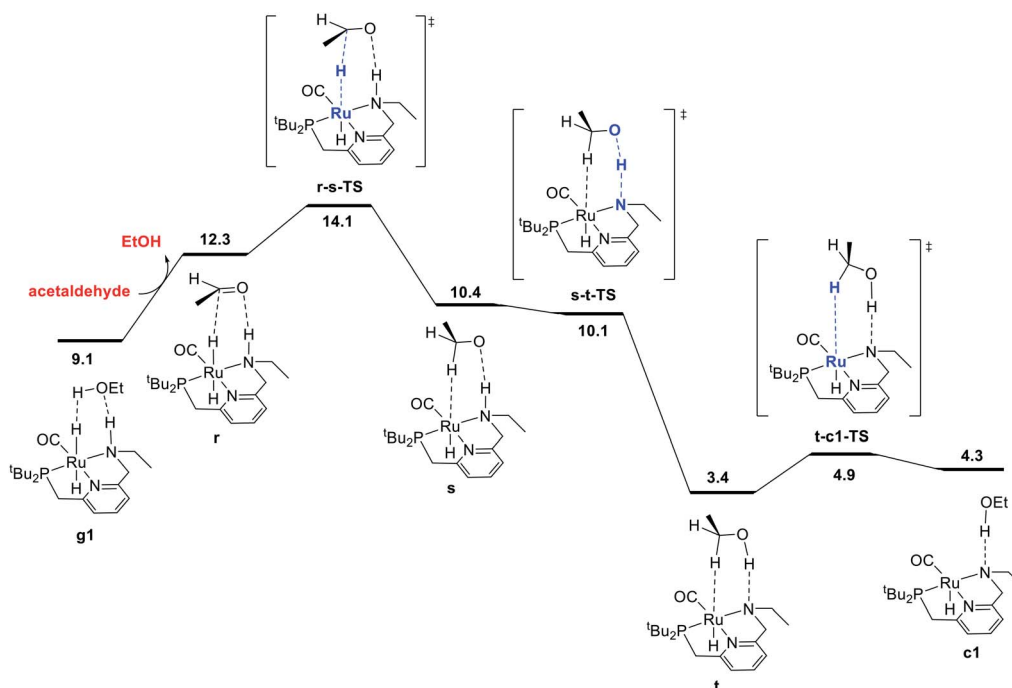


Fig. 3 MEP for hydrogenation of acetaldehyde to ethanol, accompanied by conversion of dihydride intermediate **g1** into unsaturated intermediate **c1**, which connects back to the hydrogen-activation pathway shown in Fig. 1. For consistency in this energy diagram, the free energy of intermediate **g1** (9.1 kcal mol^{−1}) is calculated based on the organic intermediates ethanol, acetaldehyde, and one molecule of hydrogen, whereas the free energy of 2.8 kcal mol^{−1} shown in Fig. 1 and 4 is based on the organic reactants ethyl acetate and two molecules of hydrogen. This presentation ensures that free energy changes within each figure are correct (e.g. the standard-state free energy change on substituting ethanol for acetaldehyde in converting from **g1** to **r** is 3.2 kcal mol^{−1} as shown in this figure).



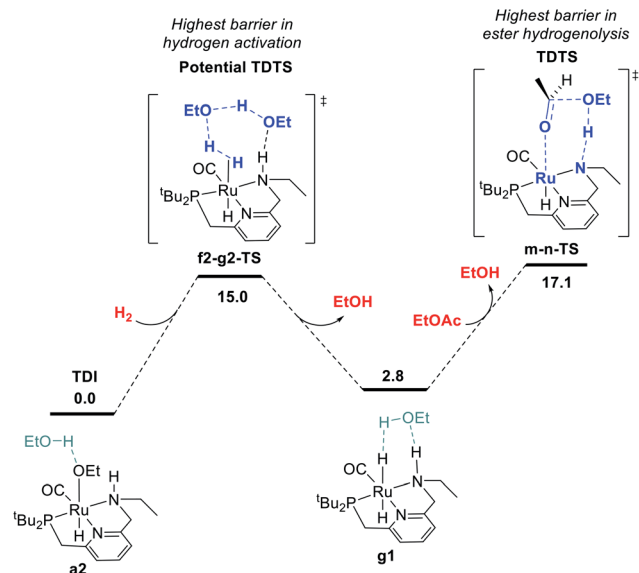


Fig. 4 Simplified energy surface determining the kinetics of ester hydrogenation.

The energetic span model allows a prediction of the rate of catalysis based on the free-energy difference between the TDI and the TDTS, which is an effective barrier for catalytic turnover.¹⁵ Taking our DFT results at face value, the TDTS is **m-n-TS** when the reactants, EtOAc and H₂, as well as the product EtOH, are at their standard states of 1 M. In this scenario, the energetic span is 17.1 kcal mol⁻¹, which is qualitatively consistent with a catalytic system that turns over rapidly at room temperature. The predicted rate law, based on the species consumed and released between the TDI and TDTS, is represented by eqn (1). In our experimental kinetic analysis described below, we have taken the above simplified model as a starting point, and additionally we find saturation behavior at high [ester], consistent with a switch to **f2-g2-TS** as TDTS under these conditions.

$$\text{rate} = k \frac{[\text{Ru}][\text{H}_2][\text{EtOAc}]}{[\text{EtOH}]^2} \quad (1)$$

Effect of explicit ethanol on kinetics

Motivated by past work showing the key involvement of protic solvent in heterolytic hydrogen cleavage²³ and by the complicated dependence of our catalytic rate on alcohol concentration (as described below), we examined the effect of including explicit ethanol molecules in the hydrogen activation and ester hydrogenolysis pathways described above. The complete pathways are included in the ESI.† Fig. 5 shows a summary of the effect of explicit ethanol molecules on the free energies of key intermediates and transition states that determine the kinetics. Taking the computed free energies at face value, several predictions can be made about the kinetics. First, the hydrido-alkoxide intermediate **a2** interacts strongly with an ethanol molecule from solution, so the “free” complex **a1** does not represent a significant fraction of the resting catalyst speciation, even at very low ethanol concentration. Second, the minimum-

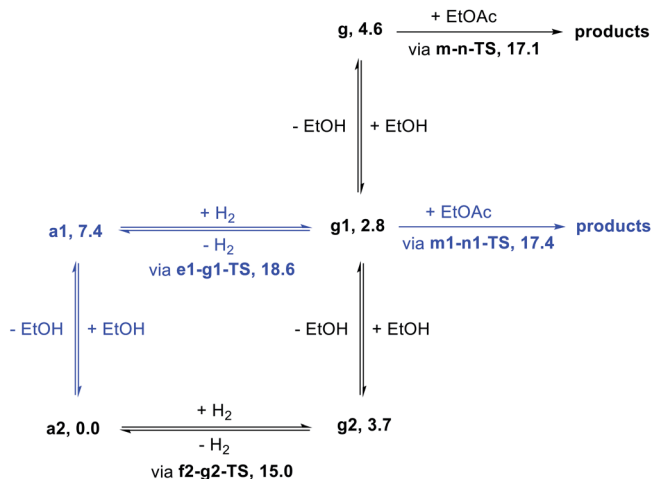


Fig. 5 Simplified kinetic model of the MEP for ester hydrogenation (black), and reasonable alternative pathways including different numbers of explicit ethanol molecules (blue). Numbers given after each species represent standard-state free energies (kcal mol⁻¹) at 298.15 K.

energy pathway for hydrogen activation goes through **f2-g2-TS** and includes two ethanol molecules as a “proton brigade”, although a pathway through **e1-g1-TS**, with only one ethanol molecule as a proton shuttle, is only 3.6 kcal mol⁻¹ higher. Third, as the energies of **g**, **g1**, and **g2** – the dihydride intermediates with 0, 1, and 2 ethanol molecules included – are above the energy of **a2** and below the energies of the transition states, their specific energies and relative ordering are not kinetically relevant. Last, ester hydrogenolysis proceeds through a very similar free-energy barrier whether an explicit ethanol molecule is included (**m1-n1-TS**, 17.4 kcal mol⁻¹) or not (**m-n-TS**, 17.1 kcal mol⁻¹). This model formed the basis for our kinetic analysis, described below.

Synthesis of proposed intermediates

RuPNN^{HEt}. The computational studies described above predict that the catalyst resting state will be a hydrido-alkoxide species such as **a2**, stabilized by hydrogen-bonding to a product alcohol molecule. Dihydride species such as **g**, **g1**, and **g2** are predicted to be key intermediates, but are less stable by several kcal mol⁻¹ and are expected to have low steady-state concentrations once even small amounts of alcohol product build up in ester hydrogenation reactions. We previously demonstrated (Scheme 2) that the precatalyst **RuPNN^{imine}** converts quantitatively to the dihydride **RuPNN^{HEt}** under hydrogen pressure,⁹ although the reversibility of this reaction on removal of hydrogen prevented easy isolation of **RuPNN^{HEt}**. Recently, Gusev reported a clever method to isolate the dihydride product **RuPNN^{H2}** formed by reaction of Milstein's original precatalyst **RuPNN^{dearom}** with hydrogen: a solution of the dearomatized species was placed under hydrogen in an unstirred pressure vessel, in a solvent mixture that dissolved **RuPNN^{dearom}** completely but allowed the product dihydride to crystallize.^{13c} Gratifyingly, we found that the same procedure

allowed us to successfully isolate **RuPNN^{HEt}** in crystalline form (Scheme 5). **RuPNN^{HEt}** is isolated as yellow crystals, which are moderately stable at room temperature, but can be stored under argon at $-37\text{ }^{\circ}\text{C}$ for extended periods without decomposition. Although **RuPNN^{HEt}** is stable even under air as a solid, it decomposes rapidly when dissolved in degassed benzene- d_6 at room temperature. As we previously characterized **RuPNN^{HEt}** fully in solution under H_2 pressure,⁹ we did not attempt to repeat the spectroscopic characterization in the absence of H_2 .

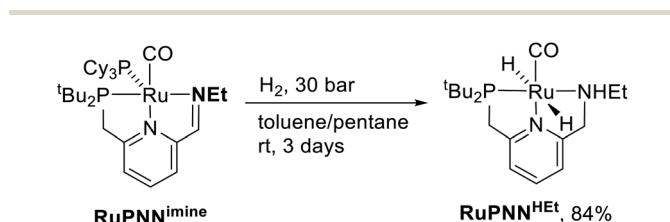
The crystals of **RuPNN^{HEt}** formed by the method described above were suitable for characterization by X-ray crystallography. Fig. 6 shows the molecular structure in the solid state. As was concluded based on our previous spectroscopic characterization,⁹ **RuPNN^{HEt}** features a nearly octahedral ruthenium(II) center bound to two hydride ligands, carbon monoxide, and a PNN-pincer ligand with an aromatic pyridine fragment flanked by $\text{CH}_2\text{P}(\text{tBu})_2$ on one side and CH_2NHET on the other. The structure is closely analogous to that of **RuPNN^{H2}** as recently reported by Gusev,^{13c} except for the change from NEt_2 to NHET . The mechanism of double hydrogenation from **RuPNN^{imine}** to give **RuPNN^{HEt}** is not obvious, and is the subject of an ongoing experimental and computational study.

RuPNN^{HOEt}. Although dihydride species such as **RuPNN^{H2}** have been proposed as the resting states in catalytic

hydrogenation reactions,^{5h,13a,24} our calculations indicate that alkoxide **a2** is more stable than the dihydride **g1** by 2.9 kcal mol^{-1} . In recent work, Gusev demonstrated experimentally that **RuPNN^{H2}** converts rapidly to alkoxide species on addition of alcohols, and showed computationally that the ethoxide species was more stable than the dihydride by 0.4 kcal mol^{-1} .^{13c} We observed analogous reactivity for **RuPNN^{HEt}**: although it decomposes in benzene- d_6 with no other additives, **RuPNN^{HEt}** rapidly converts to the hydrido-alkoxide species **RuPNN^{HOEt}** when dissolved in benzene- d_6 containing ethanol, with visible evolution of hydrogen gas (Scheme 6). NMR spectra taken immediately after reaction show one clean species. **RuPNN^{HOEt}** was fully characterized by NMR spectroscopy at $25\text{ }^{\circ}\text{C}$ in benzene- d_6 . The hydride signal appears as a doublet at -15.8 ppm . At room temperature, broad signals are observed for the methylene and hydroxyl hydrogens of free ethanol. Signals for the bound ethoxide, N-H, and the PCH_2 hydrogen *syn* to the ethoxide are not observed, as they are in rapid exchange with hydrogens from free ethanol. To characterize **RuPNN^{HOEt}** in the absence of this chemical exchange, ^1H NMR spectra were recorded from $-90\text{ }^{\circ}\text{C}$ to $20\text{ }^{\circ}\text{C}$ in toluene- d_8 (see the ESI† for spectral images). At $-50\text{ }^{\circ}\text{C}$, the above chemical exchanges are slow on the NMR time scale, and distinct resonances are observed for free ethanol, bound ethoxide, the N-H, and all four CH_2 linker hydrogens.

Single crystals of **RuPNN^{HOEt}** suitable for X-ray crystallography were obtained by slow evaporation of a pentane solution containing a small amount of ethanol. Although crystals could be reproducibly obtained in this manner, the instability of **RuPNN^{HOEt}** in the absence of an excess of ethanol coupled with its high solubility in solvents with a wide range of polarities have thus far prevented its bulk isolation as a solid. Fig. 7 shows the structure of **RuPNN^{HOEt}**. In the solid state, the ethoxide ligand is *syn* to the N-H group, which is pseudo-axial and is 2.21 \AA from the ethoxide oxygen, indicating a weak intramolecular hydrogen bond. A molecule of ethanol is present in the asymmetric unit, and the O-H hydrogen interacts with the ethoxide oxygen through hydrogen-bonding with a distance of 1.73 \AA . The solid-state geometric parameters for **RuPNN^{HOEt}** are remarkably similar to the computationally optimized structure **a2**, which was the lowest-energy hydrido-alkoxide conformation we were able to locate that included one explicit ethanol molecule.

The rapid conversion of **RuPNN^{HEt}** to **RuPNN^{HOEt}** at room temperature is consistent with our DFT study above. This transformation is the reverse of the hydrogen activation shown in Fig. 1, which is predicted to proceed in the reverse direction



Scheme 5 Synthesis of **RuPNN^{HEt}**.

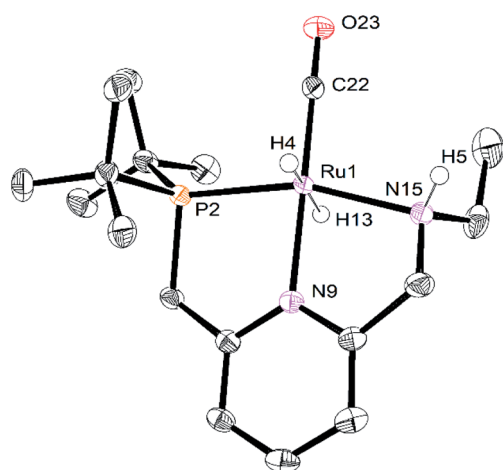
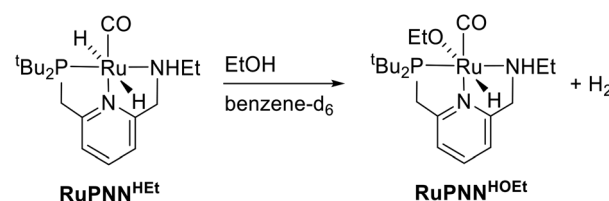


Fig. 6 ORTEP diagram of **RuPNN^{HEt}**, showing 50% probability ellipsoids. Hydrogen atoms other than Ru-H and N-H are omitted for clarity. Selected bond lengths (Angstroms) and angles (degrees): Ru(1)–P(2), 2.2536(6); Ru(1)–N(15), 2.1893(19); Ru(1)–N(9), 2.0980(19); Ru(1)–C(22), 1.830(2); C(22)–O(23), 1.164(3); P(2)–Ru(1)–N(9), 82.45(6); N(9)–Ru(1)–N(15), 78.71(7).



Scheme 6 Synthesis of **RuPNN^{HOEt}**.



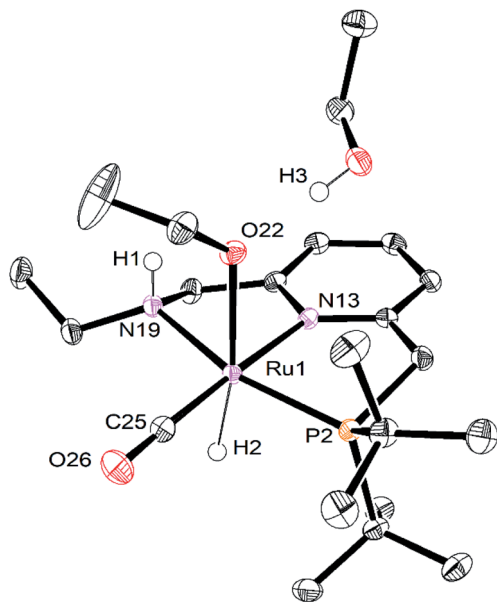


Fig. 7 ORTEP diagram of $\text{RuPNN}^{\text{HOEt}}$, showing 50% probability ellipsoids. Hydrogen atoms other than Ru–H, N–H, and O–H are omitted for clarity. Selected bond lengths (Angstroms) and angles (degrees): Ru(1)–P(2), 2.2671(5); Ru(1)–N(13), 2.1056(14); Ru(1)–N(19), 2.1693(14); Ru(1)–O(22), 2.1980(12); Ru(1)–C(25), 1.8357(19); C(25)–O(26), 1.159(2); H(1)–O(22), 1.725; H(3)–O(22), 2.212; P(2)–Ru(1)–N(13), 82.60(4); N(13)–Ru(1)–N(19), 77.78(5).

with a free-energy barrier of $12.1 \text{ kcal mol}^{-1}$, proceeding from **g1** through **f2-g2-TS**. The complete formation of $\text{RuPNN}^{\text{HOEt}}$ from $\text{RuPNN}^{\text{HEt}}$ suggested that, as predicted by computation, the alkoxide species might be more stable under catalytic conditions, and would hence represent the resting state and TDI. To confirm this, we placed a solution of $\text{RuPNN}^{\text{HOEt}}$ formed *in situ* from $\text{RuPNN}^{\text{HEt}}$ and ethanol under 10 bar H_2 in a high-pressure NMR tube. No conversion back to the dihydride species was observed, consistent with the prediction from computation that $\text{RuPNN}^{\text{HOEt}}$ is the dominant resting state throughout the catalytic reaction.

Kinetics

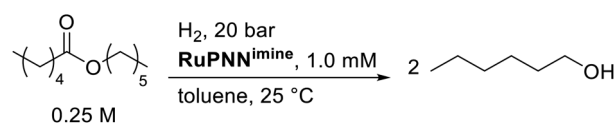
As we noted in the introduction, DFT studies of catalytic ester hydrogenation are widespread but kinetic studies are rare. Because the computed mechanism and energies make clear predictions about the kinetics, the latter provide an important check on the former. Based on our computed mechanism, the following predictions can be made. First, because hydrogen activation occurs between the TDI and TDTS, the reaction should be first-order in hydrogen. If a dihydride intermediate such as **g1** were more stable than the intermediate preceding hydrogen activation (**a2** in our work), the reaction would follow zero-order kinetics in hydrogen. Second, because an ester molecule is consumed between the TDI and TDTS, the reaction should be first-order in ester. If the barrier for hydrogen activation were much higher than the barrier for ester hydrogenolysis, the reaction would follow zero-order kinetics in ester. If these two barriers are similar in energy,

saturation behavior is possible. Third, because alcohol product is released between the TDI and TDTS, the reaction should be inhibited by the buildup of alcohol. The precise dependence of the rate on [alcohol] is not unambiguously predicted by computation, because of the multiple pathways available as shown in Fig. 5 above. Lastly, and very importantly, the overall rate of reaction should be approximately consistent with the overall barrier predicted by DFT, which is $17.1 \text{ kcal mol}^{-1}$ in our system.

Although the hydrogenation of ethyl acetate to ethanol was ideal for our computational study and for the isolation of the hydrido-alkoxide intermediate $\text{RuPNN}^{\text{HOEt}}$, we chose to conduct detailed kinetic studies using hexyl hexanoate as substrate, because both the ester reactant and alcohol product have very low volatilities at room temperature, which minimizes the possibility of evaporation of reactant or product at any point during the setup, reaction, or analysis. As both $\text{RuPNN}^{\text{HEt}}$ and $\text{RuPNN}^{\text{HOEt}}$ were unstable in solution, we conducted kinetic studies using $\text{RuPNN}^{\text{imine}}$ as precatalyst. We previously determined that isopropyl alcohol was an ideal solvent for obtaining high catalytic rates and turnover numbers in practical ester hydrogenation catalyzed by $\text{RuPNN}^{\text{imine}}$,⁹ but we decided to conduct kinetic studies in toluene for two reasons: (1) the $\text{RuPNN}^{\text{imine}}$ precatalyst is only sparingly soluble in isopropyl alcohol, posing difficulties with the preparation of stock solutions and occasionally causing clogging in the stainless-steel tubing used for removing aliquots from the reaction mixture; and (2) as described below, the hexanol product was found to inhibit turnover, and the analysis of this observed product inhibition was most straightforward if no other alcohols were present in solution.

In kinetic experiments, we monitored the conversion of hexyl hexanoate to 1-hexanol at 25°C by gas chromatography, with tetradecane as an internal standard. We began with the standard conditions shown in Scheme 7, then varied the initial concentrations of $\text{RuPNN}^{\text{imine}}$, hexyl hexanoate, and hexanol, as well as the hydrogen pressure in independent experiments. The plots labeled “without preactivation” in Fig. 8 shows a typical kinetic trace under our standard conditions. Over approximately the first 45 minutes of the reaction, the rate increases, after which apparent pseudo-first-order consumption of ester is observed, as the plot of $\ln[\text{ester}]$ vs. time is linear after this point. During the 45 minute induction period, aliquots are dark purple, indicating the presence of the strongly absorbing precatalyst $\text{RuPNN}^{\text{imine}}$, and become pale yellow as the precatalyst is converted to the resting state, which we propose is a hydrido-hexyloxy species analogous to $\text{RuPNN}^{\text{HOEt}}$.

To determine if the observed induction period can be explained by the activation of $\text{RuPNN}^{\text{imine}}$ with hydrogen, we



Scheme 7 Standard conditions for kinetic experiments.



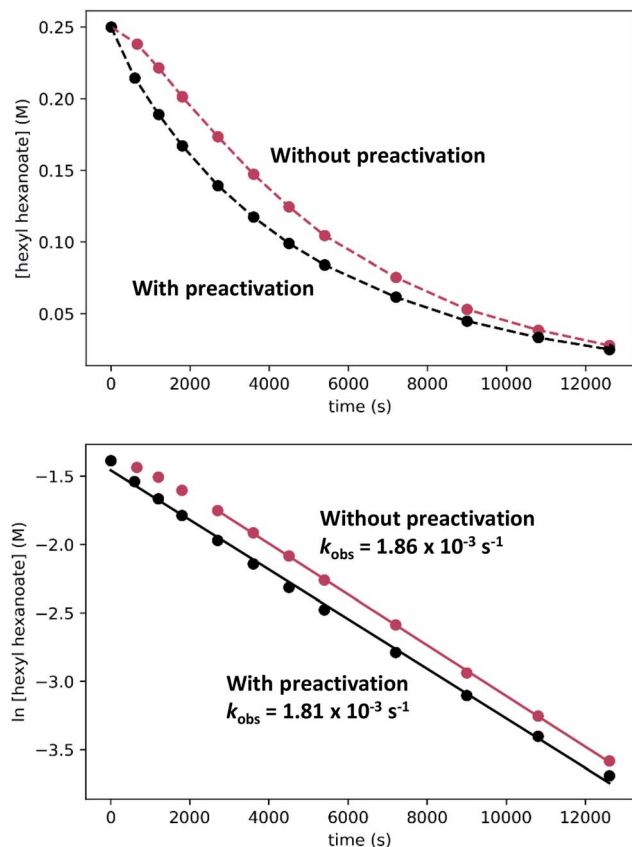


Fig. 8 Comparison of hexyl hexanoate hydrogenation catalyzed by $\text{RuPNN}^{\text{imine}}$ with and without preactivation of the catalyst by incubation under 20 bar hydrogen for 90 minutes. The top plots show $[\text{ester}]$ vs. time; dashed lines are merely to guide the eye and do not represent a fit to the data. The bottom plots show $\ln[\text{ester}]$ vs. time, with linear fits to all data (with preactivation) or to the time points from 45 minutes on (without preactivation).

conducted a preactivation experiment where we first pressurized a solution of $\text{RuPNN}^{\text{imine}}$ with hydrogen (20 bar) for 90 minutes, which results in formation of the dihydride complex $\text{RuPNN}^{\text{HET}}$.⁹ Then, the hexyl hexanoate substrate was transferred into the pressure reactor and its conversion to 1-hexanol was monitored at 25 °C. As the plots labeled “with preactivation” in Fig. 8 demonstrate, the reaction follows apparent first-order kinetics without an induction period, giving a nearly identical k_{obs} value to what is observed without pre-activation of the catalyst. Importantly, this experiment rules out the possibility that sigmoidal kinetics come from acceleration of the reaction by the product alcohol, as proposed by O and Morris for their catalyst.^{5a} We also attempted to use $\text{RuPNN}^{\text{HET}}$ directly as a precatalyst, but partial decomposition prior to the introduction of hydrogen pressure hindered our attempts to obtain reliable kinetic data. Because it was much more operationally convenient to assemble kinetic experiments in parallel without a catalyst preactivation step, we elected to conduct further kinetic trials using $\text{RuPNN}^{\text{imine}}$ as the precatalyst, using only the data after the 45 minute induction period to develop the kinetic model for the activated catalyst.

To determine the partial order in catalyst concentration under the standard conditions, we repeated the experiment with a range of initial concentrations of $\text{RuPNN}^{\text{imine}}$ (Fig. 9). The same initial induction period followed by pseudo-first-order behavior was observed, and k_{obs} was taken as the slope of the linear portion of the plot of $\ln[\text{ester}]$ vs. time. A plot of k_{obs} vs. $[\text{RuPNN}^{\text{imine}}]_0$ is linear with an intercept of zero, indicating that the reaction is first-order in [ruthenium] after the induction period is complete.

To determine the partial order in hydrogen, we repeated the standard experiment varying the hydrogen pressure (Fig. 10). In all experiments, a constant hydrogen pressure was maintained as aliquots were removed. Again, k_{obs} was determined based on the linear portion of the plot of $\ln[\text{ester}]$ vs. time, and again a plot of k_{obs} vs. hydrogen pressure gave a line with an intercept of zero, indicating that the reaction is first-order in hydrogen under these conditions.

We then repeated the experiment with initial ester (hexyl hexanoate) concentrations varied over a wide range from 0.05 M to 0.75 M. At high $[\text{ester}]_0$, we observed a change from pseudo-first-order to pseudo-zero-order behavior, consistent with saturation kinetics. When $[\text{ester}]_0$ is 0.25 M or less, apparent first-order kinetic behavior is observed in each individual

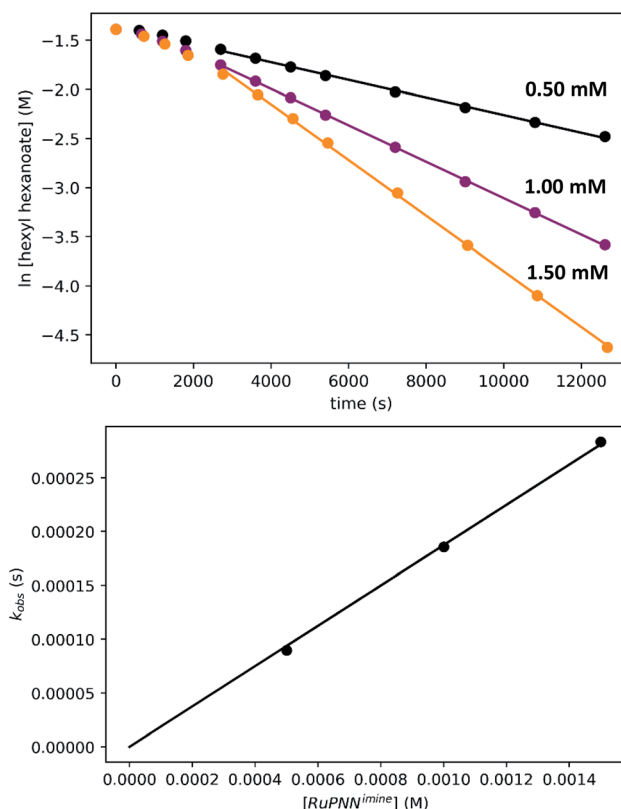


Fig. 9 Determination of the partial order in $\text{RuPNN}^{\text{imine}}$ under the standard conditions. The top plots show the time course of ester conversion using different initial concentrations of $\text{RuPNN}^{\text{imine}}$, along with linear fits to the logarithm of $[\text{ester}]$, using data after the induction period of 45 minutes. The bottom plot shows the linear relationship between k_{obs} and $[\text{RuPNN}^{\text{imine}}]$.



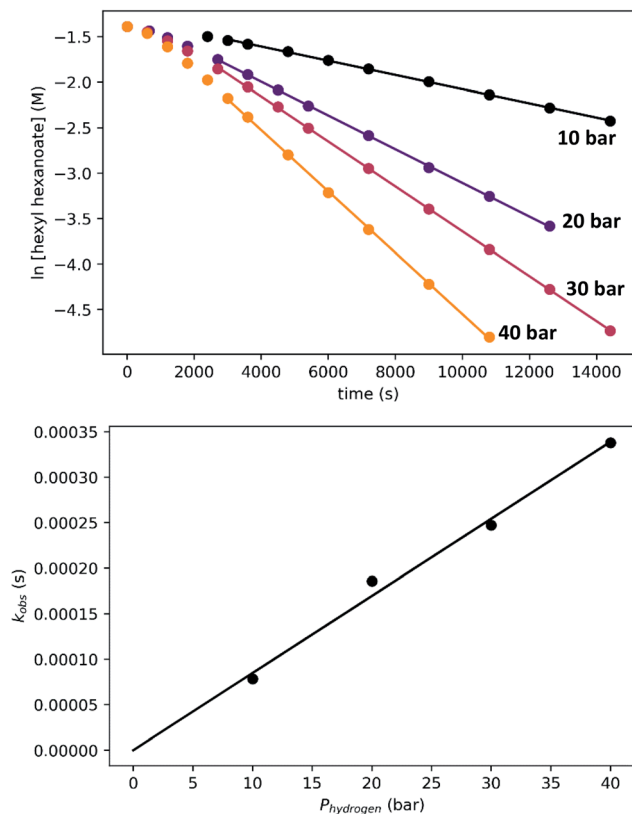


Fig. 10 Determination of the partial order in hydrogen under the standard conditions. The top plots show the time course of ester conversion, along with linear fits to the logarithm of [ester], using data after the induction period of 45 minutes. The bottom plot shows the linear relationship between k_{obs} and hydrogen pressure.

experiment, but k_{obs} increases dramatically at lower $[\text{ester}]_0$, consistent with inhibition by the product 1-hexanol. Although it may be counterintuitive that pseudo-first-order kinetic behavior in [ester] is observed when the buildup of alcohol product inhibits the reaction, in our system the increasing product inhibition is roughly cancelled out by saturation in [ester], resulting in apparent first-order behavior in each experiment. To directly probe for inhibition by the product hexanol, we repeated the experiment with a range of initial 1-hexanol concentrations, and we found that the rate decreases as $[\text{hexanol}]_0$ is increased, consistent with product inhibition.

To deconvolute the effects of saturation in [ester] and inhibition by the product alcohol, we developed a numerical model of the reaction progress using the program Copasi.²⁵ Numerical modeling is seeing increased use in the analysis of kinetics in catalytic systems.^{16b,26} When used in combination with DFT, kinetic modeling offers the potential to validate mechanisms and refine the energies predicted by DFT.^{16b,26c} In developing our model, we included the data after the 45 minute induction period from a total of 18 kinetic experiments, where the initial ester, alcohol, and ruthenium concentrations were varied, as well as the hydrogen pressure. Our model takes the standard-state free energies of the kinetically relevant intermediates and transition states as inputs (see Fig. 5 above), and computes

the time course for ester hydrogenation, given the initial concentrations of ruthenium catalyst (**a2**), hexyl hexanoate, hexanol, and hydrogen. Hydrogen concentration, calculated from its known solubility in toluene at 25 °C and the appropriate pressure,²⁷ was held fixed in the model. Because the activity coefficients of alcohols are known to vary significantly over the range of 0 to 1.0 M in non-polar solvents,²⁸ we used the activity of 1-hexanol rather than its molarity, as estimated following a model developed by Li and coworkers for 1-hexanol in benzene.²⁹

In attempting to reproduce the kinetic data with our model, we set the relative free energy of **a2** to zero and compared a range of scenarios adjusting the remaining energies, in an attempt to achieve the best overall fit while including the smallest number of adjustable parameters. We found no better fit by allowing the free energies of **a1**, **e1-g1-TS**, **g2**, **g1**, or **g** to be adjusted. On the other hand, allowing adjustment of **f2-g2-TS**, **m-n-TS**, and **m1-n1-TS** was essential to obtaining a good global fit. Further, entirely excluding the pathway through **e1-g1-TS** had no detrimental effect on the fit. Our optimized model is depicted in Fig. 11, and the global fit to the kinetic data is shown in Fig. 12. The free energies of the dihydride species **g**, **g1**, and **g2** were taken from the DFT results and held constant. The free energies of the transition states **f2-g2-TS**, **m-n-TS**, and **m1-n1-TS** were allowed to vary; fitted values are shown in Fig. 11.

Overall, the kinetic data are very well-reproduced by this simplified model, with minimal adjustment of the free energies obtained from DFT. Interestingly, the free energy of the hydrogen activation transition state **f2-g2-TS** was adjusted upward by 2.4 kcal mol⁻¹, while the energies of the ester hydrogenolysis transition states were adjusted downward by 1.2 and 1.4 kcal mol⁻¹, indicating that the standard-state activation barrier for hydrogen cleavage is the higher of the two, in contrast to the prediction from DFT. The model correctly

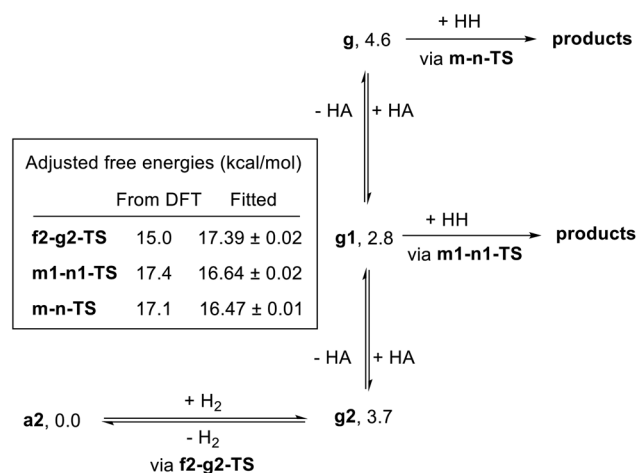


Fig. 11 Optimized kinetic model. The free energies of **a2**, **g2**, **g1**, and **g** were held fixed at the indicated values. The free energies of **f2-g2-TS**, **m-n-TS**, and **m1-n1-TS** were adjusted to achieve the best global fit to the kinetic data. HH refers to hexyl hexanoate and HA refers to 1-hexanol.

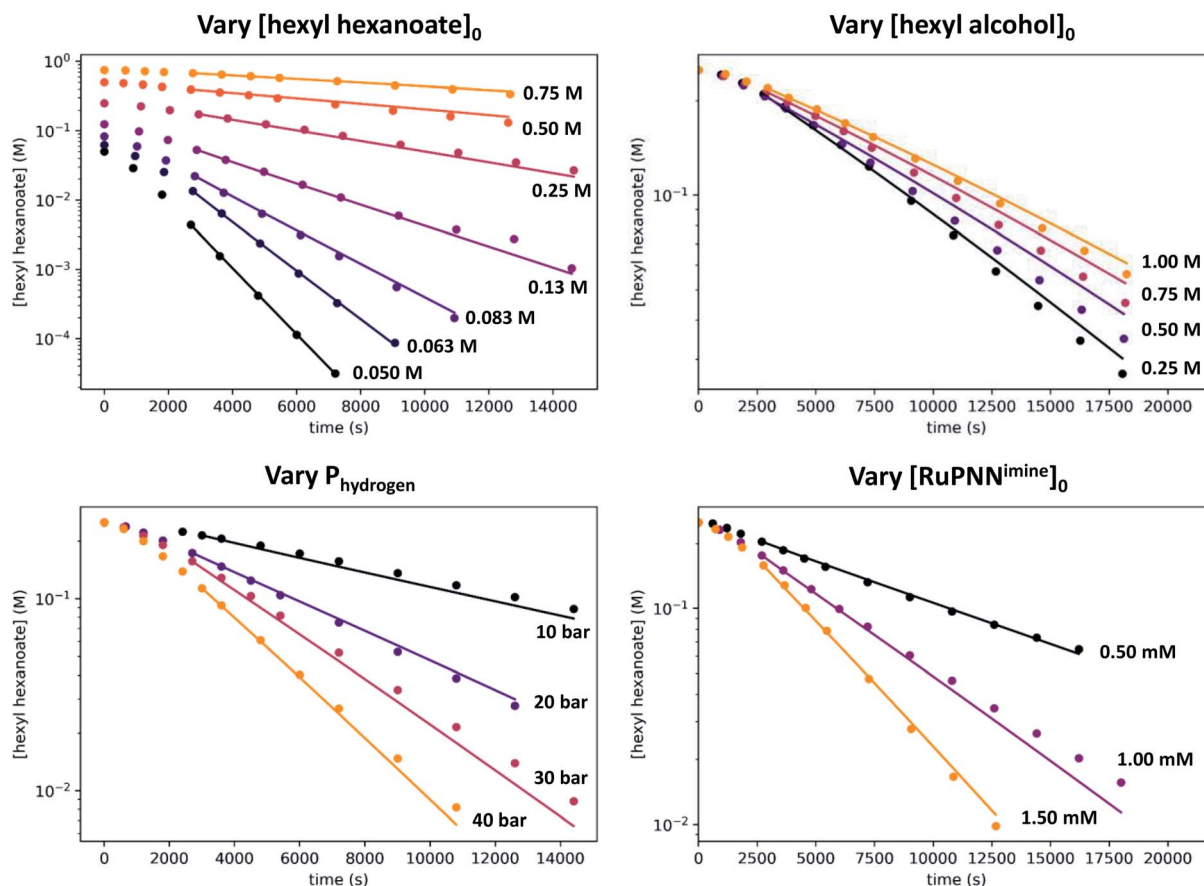


Fig. 12 Data (points) and global fit (lines) for all 18 kinetic experiments. In the standard conditions, $[\text{hexyl hexanoate}]_0 = 0.25 \text{ M}$, $[\text{hexyl alcohol}]_0 = 0 \text{ M}$, $[\text{RuPNNimine}]_0 = 1.00 \text{ mM}$, and $P_{\text{hydrogen}} = 20 \text{ bar}$. The global fit was based on all data from 45 minutes on in each kinetic experiment. Note that the vertical axes are plotted logarithmically.

reproduces the first-order dependence on hydrogen pressure, the first-order dependence on $[\text{Ru}]$, and the saturation kinetics in $[\text{ester}]$. The inclusion of two similar-barrier pathways for ester hydrogenolysis allows a transition from second-order inhibition by alcohol at low $[\text{alcohol}]$ to first-order inhibition at higher $[\text{alcohol}]$, consistent with the data. Importantly, the relatively small adjustment of the transition-state energies, less than 3 kcal mol^{-1} in each case, indicates that the barriers from DFT calculations are consistent with overall rate of the catalytic reaction. The above model satisfactorily reproduces the effect of $[\text{hexanol}]$ on the rate of reaction essentially by assuming strong hydrogen bonding to the resting state **a2** and weaker interaction with the transition states for ester hydrogenation. However, we do not claim that this model fully accounts for the behavior of the alcohol in the system, which likely includes medium polarity effects and more complicated interactions with the reacting species.

Effect of added isopropyl alcohol

Although we have conducted the above kinetic experiments in toluene, we determined previously⁹ that isopropyl alcohol was an ideal solvent for the reaction, giving rates approximately 2–3 times faster than toluene and THF. To probe the accelerating

effect of isopropyl alcohol further, we repeated our standard kinetic experiment with varying amounts of isopropyl alcohol added, up to 0.75 M. For comparison, pure isopropyl alcohol is 13.1 M. As shown in Fig. 13, we observe moderate but clear acceleration of the reaction with added isopropyl alcohol, consistent with our prior findings and in contrast with the inhibiting effect of added 1-hexanol. Although we have not tried to probe this effect further, it likely originates from a different balance of stabilization of the resting state and transition-states by the two alcohols, potentially through specific interactions and/or medium polarity effects. For example, the activity coefficient of 1-hexanol is expected to decrease with increasing $[\text{isopropyl alcohol}]$, which should reduce 1-hexanol inhibition and accelerate the catalytic reaction. We note that the detailed rate dependence determined above for hexyl hexanoate, especially the effect of the alcohol, does not necessarily extend to the hydrogenation of all other esters.

Disproportionation of aldehydes to esters

As Gusev has reported recently,³⁰ catalysts for ester hydrogenation that produce an aldehyde intermediate can also be active for the catalytic disproportionation of aldehydes to esters, which effectively operates by running the ester hydrogenolysis



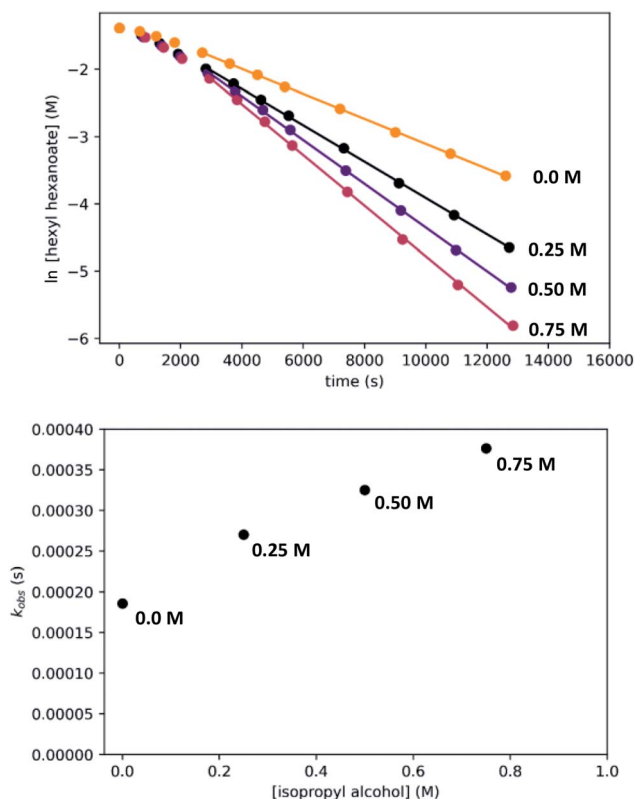
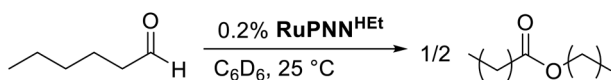


Fig. 13 Effect of added isopropyl alcohol on the hydrogenation of hexyl hexanoate. The top plots show the time course of ester conversion using different initial concentrations of isopropyl alcohol, along with linear fits to the logarithm of [ester], using data after the induction period of 45 minutes. The bottom plot shows k_{obs} vs. [isopropyl alcohol].

pathway in reverse and the aldehyde hydrogenation pathway in the forward direction. Rearranging the pathways in Fig. 2 and 3 gives the MEP shown in Fig. S16 in the ESI,[†] with an overall barrier of 12.9 kcal mol⁻¹. Therefore, our calculations predict that aldehyde disproportionation should be rapid at room temperature. To test this prediction, we dissolved 1-hexanal in benzene-d₆ with 0.2 mol% **RuPNN^{H₂Et}** at room temperature, and monitored by ¹H NMR. After 10 minutes, the aldehyde was completely consumed and hexyl hexanoate was the major product (Scheme 8). Further studies of this disproportionation reaction are in progress.

Discussion

We previously demonstrated that the ubiquitous **RuPNN^{dearom}** is not kinetically competent as a catalyst for ester hydrogenation, instead converting from an inactive precatalytic form with an NEt₂ side group to an active form **RuPNN^{H₂Et}**, which features



Scheme 8 Disproportionation of 1-hexanal.

an NH₂ group that is essential for catalytic activity.⁹ In this work, we have presented a plausible minimum-energy pathway, identified through computation and validated experimentally through kinetic characterization and isolation of two key intermediates, **RuPNN^{H₂Et}** and **RuPNN^{HOEt}**. Our computations demonstrate that the N–H functional group plays a key role in the exceptional room-temperature activity of this catalyst. The N–H group is deprotonated and re-protonated in our MEPs for hydrogen activation, ester hydrogenolysis, and aldehyde hydrogenation, although in the first two cases we identified nearly isoenergetic pathways where the N–H group acts only as a hydrogen-bond donor without being deprotonated. A thorough search for alternative pathways where a CH₂ linker is involved in hydrogen activation identified a minimum barrier of 23.7 kcal mol⁻¹, compared to 15.0 in our MEP.

Because of the widespread application of **RuPNN^{dearom}** in catalytic transformations and the corresponding widespread study of its reactivity by DFT prior to our disclosure of its facile dehydroalkylative activation, this system provides a unique case study in how the application of DFT in the absence of complementary experimental data can lead to the proposal of incorrect reaction mechanisms. Three studies we are aware of report a complete pathway for ester hydrogenation catalyzed by **RuPNN^{dearom}**. In 2017, Zhang and coworkers reported a mechanism for the hydrogenation of ethyl benzoate catalyzed by **RuPNN^{dearom}**.^{13b} In their work, **RuPNN^{dearom}** was identified as the resting state, and the highest barrier occurred in ester hydrogenolysis, giving an energetic span of 27.2 kcal mol⁻¹. In 2011, Wang and coworkers reported a study comparing the activity of **RuPNN^{dearom}** for the acceptorless dehydrogenative coupling (ADC) of alcohols to give esters against the coupling of amines and alcohols to give amides, rationalizing the preference for the latter pathway over the former.^{13a} Reversing the ADC process predicts an overall energetic span of 38.5 kcal mol⁻¹ for ester hydrogenation, from a dihydride resting state after hydrogen activation to a proton-transfer TDTS along the ester hydrogenolysis pathway. In 2020, Gusev reported a revised mechanism for ester hydrogenation and the reverse ADC, aided by the experimental identification of a hydridoalkoxide species as the proposed resting state.^{13c} In that study, the energetic span from the hydridoalkoxide TDI to the TDTS, a Hasanayn-like²¹ hydride-alkoxide metathesis transition state, was 31.8 kcal mol⁻¹.

As all three of the above studies rely on the on-cycle intermediacy of either **RuPNN^{dearom}**, **RuPNN^{H₂Et}**, or both, the proposed mechanisms cannot be correct, as we have shown that **RuPNN^{dearom}**, which converts rapidly to **RuPNN^{H₂Et}** under hydrogen pressure,¹ is inactive in ester hydrogenation prior to undergoing dehydroalkylation.⁹ With our present demonstration that the experimental free-energy barrier to catalytic turnover is only 17.4 kcal mol⁻¹, the computed pathways above can also be excluded because the barriers they predict are implausibly high. Although it is not always explicitly stated, a common filter for the plausibility of reaction mechanisms calculated by DFT or other quantum-chemistry methods is a qualitative agreement of the overall reaction barrier with the observed rate of reaction. When detailed kinetic information is not available,

reaction barriers must be estimated knowing only the catalyst loading, reaction time, and temperature. In the case of ester hydrogenation catalyzed by **RuPNN^{dearom}**, Milstein's initial disclosure reported a turnover number of 100 in 4 h at 115 °C.¹ If one assumes that catalyst induction is rapid and the turnover frequency is constant over the reaction time course, an overall barrier (energetic span) of 26.7 kcal mol⁻¹ can be estimated. However, the barrier for turnover can be substantially overestimated if the catalyst undergoes a slow activation followed by very rapid turnover, as we showed is the case for this system.⁹ This overestimation makes the above mechanisms, especially those proposed by Gusev and Zhang, appear plausible even though they predict barriers that are much higher than the actual barrier for catalytic turnover.

It is worth revisiting a broader implication of the findings we report here. As we described in the introduction, the majority of elite catalysts for ester hydrogenation and the reverse ADC of alcohols feature an N–H group with a key role in promoting catalysis. In this work and in a prior study,⁹ we demonstrated that Milstein's catalyst **RuPNN^{dearom}** and NEt₂-substituted CNN-pincer analogs developed in our group^{7d} are initially inactive, and must convert to an NHEt form to be catalytically active. Recently, Khaskin, Gusev, and coworkers²² have shown that the same is true for a related bipyridyl PNN-pincer catalyst originally reported by Milstein and coworkers.³¹ In this case, a pyridine ring is hydrogenated to a piperidine, again providing a latent N–H functional group with a key role in catalysis. Before these reports, initial proposals^{1,2,31} and many computational studies^{13a,14} pointed to the reversible deprotonation of a CH₂ linker as a key step in catalysis, but these proposals should potentially be reevaluated in light of the new findings. Importantly, our work does not completely rule out the potential involvement of CH₂ linkers in other processes. It is experimentally known that the addition of H₂ to **RuPNN^{dearom}** occurs reversibly at room temperature (Scheme 1).¹ Our calculations (Fig. S7†) indicate that this process has a barrier of 23.7 kcal mol⁻¹ under the conditions of ester hydrogenation, which is too high to account for the fast room-temperature turnover the activated catalyst exhibits in this process, but could be accessible at a higher temperature in a different process. We are continuing to probe these possibilities in computational and experimental studies of related catalytic transformations.

Conclusion

We previously demonstrated that Milstein's pincer–ruthenium catalyst for ester hydrogenation and related reactions is activated by dehydroalkylation to give the active form, which contains an NH functional group that is essential for catalysis.⁹ In this work, we have presented a detailed computational and experimental study of the mechanism of ester hydrogenation catalyzed by this activated form, and conclude that participation of the N–H functional group is key in hydrogen activation, ester hydrogenolysis, and aldehyde hydrogenation. The catalyst speciation, the overall rate of reaction, and the dependence of the rate on the concentrations of reactants and products

determined by experiment are in agreement with the mechanism predicted by DFT.

Author contributions

J. Pham: kinetic experiments, Copasi modeling, writing of manuscript. C. Jarczyk: DFT calculations, synthesis. E. Reynolds: DFT calculations, synthesis. S. Kelly: DFT calculations. T. Kim: DFT calculations. T. He: kinetic experiments, synthesis, DFT calculations. J. Keith: funding acquisition, supervision of computational work, review and editing of manuscript. A. Chianese: conceptualization, funding acquisition, and supervision; writing, review, and editing of manuscript.

Conflicts of interest

The authors declare no competing financial interest.

Acknowledgements

We thank the National Science Foundation (CHE-1665144 and CHE-1954924) for support of the research project, and (CHE-1726308) for the acquisition of an upgraded NMR spectrometer.

References

- 1 J. Zhang, G. Leituss, Y. Ben-David and D. Milstein, *Angew. Chem., Int. Ed.*, 2006, **45**, 1113–1115.
- 2 J. Zhang, G. Leituss, Y. Ben-David and D. Milstein, *J. Am. Chem. Soc.*, 2005, **127**, 10840–10841.
- 3 (a) C. Gunanathan, Y. Ben-David and D. Milstein, *Science*, 2007, **317**, 790–792; (b) B. Gnanaprakasam, E. Balaraman, Y. Ben-David and D. Milstein, *Angew. Chem., Int. Ed.*, 2011, **50**, 12240–12244; (c) H. Zeng and Z. Guan, *J. Am. Chem. Soc.*, 2011, **133**, 1159–1161; (d) J. W. Rigoli, S. A. Moyer, S. D. Pearce and J. M. Schomaker, *Org. Biomol. Chem.*, 2012, **10**, 1746–1749; (e) B. Gnanaprakasam and D. Milstein, *J. Am. Chem. Soc.*, 2011, **133**, 1682–1685; (f) B. Gnanaprakasam, Y. Ben-David and D. Milstein, *Adv. Synth. Catal.*, 2010, **352**, 3169–3173; (g) E. Balaraman, C. Gunanathan, J. Zhang, L. J. W. Shimon and D. Milstein, *Nat. Chem.*, 2011, **3**, 609–614; (h) C. A. Huff and M. S. Sanford, *ACS Catal.*, 2013, **3**, 2412–2416; (i) M. B. Chaudhari, G. S. Bisht, P. Kumari and B. Gnanaprakasam, *Org. Biomol. Chem.*, 2016, **14**, 9215–9220.
- 4 (a) L. A. Saudan, C. M. Saudan, C. Debieux and P. Wyss, *Angew. Chem., Int. Ed.*, 2007, **46**, 7473–7476; (b) D. Spasyuk and D. G. Gusev, *Organometallics*, 2012, **31**, 5239–5242; (c) D. Spasyuk, S. Smith and D. G. Gusev, *Angew. Chem., Int. Ed.*, 2013, **52**, 2538–2542; (d) W. Li, J.-H. Xie, M.-L. Yuan and Q.-L. Zhou, *Green Chem.*, 2014, **16**, 4081–4085; (e) G. A. Filonenko, M. J. B. Aguilá, E. N. Schulpen, R. van Putten, J. Wiecko, C. Müller, L. Lefort, E. J. M. Hensen and E. A. Pidko, *J. Am. Chem. Soc.*, 2015, **137**, 7620–7623; (f) D. Spasyuk, C. Vicent and D. G. Gusev, *J. Am. Chem. Soc.*, 2015, **137**, 3743–3746; (g) X. Tan, Q. Wang, Y. Liu, F. Wang, H. Lv and X. Zhang, *Chem. Commun.*, 2015, **51**, 12193–



- 12196; (h) X. Tan, Y. Wang, Y. Liu, F. Wang, L. Shi, K. H. Lee, Z. Lin, H. Lv and X. Zhang, *Org. Lett.*, 2015, **17**, 454–457; (i) Z. Wang, X. Chen, B. Liu, Q.-B. Liu, G. A. Solan, X. Yang and W.-H. Sun, *Catal. Sci. Technol.*, 2017, **7**, 1297–1304.
- 5 (a) W. W. N. O and R. H. Morris, *ACS Catal.*, 2013, **3**, 32–40; (b) T. Otsuka, A. Ishii, P. A. Dub and T. Ikariya, *J. Am. Chem. Soc.*, 2013, **135**, 9600–9603; (c) S. Chakraborty, P. O. Lagaditis, M. Förster, E. A. Bielinski, N. Hazari, M. C. Holthausen, W. D. Jones and S. Schneider, *ACS Catal.*, 2014, **4**, 3994–4003; (d) T. Chen, H. Li, S. Qu, B. Zheng, L. He, Z. Lai, Z.-X. Wang and K.-W. Huang, *Organometallics*, 2014, **33**, 4152–4155; (e) K. Junge, B. Wendt, H. Jiao and M. Beller, *ChemCatChem*, 2014, **6**, 2810–2814; (f) S. Qu, H. Dai, Y. Dang, C. Song, Z.-X. Wang and H. Guan, *ACS Catal.*, 2014, **4**, 4377–4388; (g) S. Werkmeister, K. Junge, B. Wendt, E. Alberico, H. Jiao, W. Baumann, H. Junge, F. Gallou and M. Beller, *Angew. Chem., Int. Ed.*, 2014, **53**, 8722–8726; (h) X. Chen, Y. Jing and X. Yang, *Chem.–Eur. J.*, 2016, **22**, 1950–1957; (i) D. G. Gusev, *ACS Catal.*, 2016, **6**, 6967–6981; (j) R. van Putten, E. A. Uslamin, M. Garbe, C. Liu, A. Gonzalez-de-Castro, M. Lutz, K. Junge, E. J. M. Hensen, M. Beller, L. Lefort and E. A. Pidko, *Angew. Chem., Int. Ed.*, 2017, **56**, 7531–7534.
- 6 (a) P. A. Dub, N. J. Henson, R. L. Martin and J. C. Gordon, *J. Am. Chem. Soc.*, 2014, **136**, 3505–3521; (b) P. A. Dub and J. C. Gordon, *Dalton Trans.*, 2016, **45**, 6756–6781; (c) P. A. Dub, B. L. Scott and J. C. Gordon, *J. Am. Chem. Soc.*, 2017, **139**, 1245–1260; (d) D. J. Tindall, M. Menche, M. Schelwies, R. A. Paciello, A. Schafer, P. Comba, F. Rominger, A. S. K. Hashmi and T. Schaub, *Inorg. Chem.*, 2020, **59**, 5099–5115.
- 7 (a) C. del Pozo, M. Iglesias and F. Sánchez, *Organometallics*, 2011, **30**, 2180–2188; (b) Y. Sun, C. Koehler, R. Tan, V. T. Annibale and D. Song, *Chem. Commun.*, 2011, **47**, 8349–8351; (c) D. Kim, L. Le, M. J. Drance, K. H. Jensen, K. Bogdanovski, T. N. Cervarich, M. G. Barnard, N. J. Pudalov, S. M. M. Knapp and A. R. Chianese, *Organometallics*, 2016, **35**, 982–989; (d) L. Le, J. Liu, T. He, D. Kim, E. J. Lindley, T. N. Cervarich, J. C. Malek, J. Pham, M. R. Buck and A. R. Chianese, *Organometallics*, 2018, **37**, 3286–3297.
- 8 L. Le, J. Liu, T. He, J. C. Malek, T. N. Cervarich, J. C. Buttner, J. Pham, J. M. Keith and A. R. Chianese, *Organometallics*, 2019, **38**, 3311–3321.
- 9 T. He, J. C. Buttner, E. F. Reynolds, J. Pham, J. C. Malek, J. M. Keith and A. R. Chianese, *J. Am. Chem. Soc.*, 2019, **141**, 17404–17413.
- 10 E. Fogler, J. A. Garg, P. Hu, G. Leituss, L. J. W. Shimon and D. Milstein, *Chem.–Eur. J.*, 2014, **20**, 15727–15731.
- 11 (a) S. Takebayashi and S. H. Bergens, *Organometallics*, 2009, **28**, 2349–2351; (b) I. Carpenter, S. C. Eckelmann, M. T. Kuntz, J. A. Fuentes, M. B. France and M. L. Clarke, *Dalton Trans.*, 2012, **41**, 10136–10140; (c) J. A. Fuentes, S. M. Smith, M. T. Scharbert, I. Carpenter, D. B. Cordes, A. M. Z. Slawin and M. L. Clarke, *Chem.–Eur. J.*, 2015, **21**, 10851–10860; (d) O. Ogata, Y. Nakayama, H. Nara, M. Fujiwara and Y. Kayaki, *Org. Lett.*, 2016, **18**, 3894–3897.
- 12 (a) W. Kuriyama, Y. Ino, O. Ogata, N. Sayo and T. Saito, *Adv. Synth. Catal.*, 2010, **352**, 92–96; (b) J. Zhang, E. Balaraman, G. Leituss and D. Milstein, *Organometallics*, 2011, **30**, 5716–5724; (c) D. Spasyuk, S. Smith and D. G. Gusev, *Angew. Chem., Int. Ed.*, 2012, **51**, 2772–2775; (d) C. Ziebart, R. Jackstell and M. Beller, *ChemCatChem*, 2013, **5**, 3228–3231; (e) S. Chakraborty, H. Dai, P. Bhattacharya, N. T. Fairweather, M. S. Gibson, J. A. Krause and H. Guan, *J. Am. Chem. Soc.*, 2014, **136**, 7869–7872; (f) T. vom Stein, M. Meuresch, D. Limper, M. Schmitz, M. Holscher, J. Coetzee, D. J. Cole-Hamilton, J. Klankermayer and W. Leitner, *J. Am. Chem. Soc.*, 2014, **136**, 13217–13225; (g) T. J. Korstanje, J. I. van der Vlugt, C. J. Elsevier and B. de Bruin, *Science*, 2015, **350**, 298–302; (h) T. P. Brewster, N. M. Rezayee, Z. Culakova, M. S. Sanford and K. I. Goldberg, *ACS Catal.*, 2016, **6**, 3113–3117; (i) N. A. Espinosa-Jalapa, A. Nerush, L. J. W. Shimon, G. Leituss, L. Avram, Y. Ben-David and D. Milstein, *Chem.–Eur. J.*, 2017, **23**, 5934–5938; (j) J. Yuwen, S. Chakraborty, W. W. Brennessel and W. D. Jones, *ACS Catal.*, 2017, **7**, 3735–3740; (k) A. Anaby, M. Schelwies, J. Schwaben, F. Rominger, A. S. K. Hashmi and T. Schaub, *Organometallics*, 2018, **37**, 2193–2201.
- 13 (a) H. Li, X. Wang, F. Huang, G. Lu, J. Jiang and Z.-X. Wang, *Organometallics*, 2011, **30**, 5233–5247; (b) H. Wang, C. Liu and D. Zhang, *Mol. Catal.*, 2017, **440**, 120–132; (c) D. G. Gusev, *Organometallics*, 2020, **39**, 258–270.
- 14 (a) G. Zeng and S. Li, *Inorg. Chem.*, 2011, **50**, 10572–10580; (b) H. Li, M. Wen and Z.-X. Wang, *Inorg. Chem.*, 2012, **51**, 5716–5727; (c) X. Yang, *ACS Catal.*, 2012, **2**, 964–970; (d) D. Cho, K. C. Ko and J. Y. Lee, *Organometallics*, 2013, **32**, 4571–4576; (e) F. Hasanayn, A. Baroudi, A. A. Bengali and A. S. Goldman, *Organometallics*, 2013, **32**, 6969–6985; (f) F. Hasanayn and H. Harb, *Inorg. Chem.*, 2014, **53**, 8334–8349; (g) L. Li, M. Lei, L. Liu, Y. Xie and H. F. Schaefer, *Inorg. Chem.*, 2018, **57**, 8778–8787; (h) S. Shu, M. Huang, J. Jiang, L.-B. Qu, Y. Liu and Z. Ke, *Catal. Sci. Technol.*, 2019, **9**, 2305–2314.
- 15 S. Kozuch and S. Shaik, *Acc. Chem. Res.*, 2010, **44**, 101–110.
- 16 (a) C. Kubis, M. Sawall, A. Block, K. Neymeyr, R. Ludwig, A. Borner and D. Selent, *Chemistry*, 2014, **20**, 11921–11931; (b) E. N. Szlapa and J. N. Harvey, *Chem.–Eur. J.*, 2018, **24**, 17096–17104; (c) A. C. Brezny and C. R. Landis, *ACS Catal.*, 2019, **9**, 2501–2513.
- 17 (a) H. Nakatsuka, T. Yamamura, Y. Shuto, S. Tanaka, M. Yoshimura and M. Kitamura, *J. Am. Chem. Soc.*, 2015, **137**, 8138–8149; (b) S. Nakane, T. Yamamura, S. K. Manna, S. Tanaka and M. Kitamura, *ACS Catal.*, 2018, **8**, 11059–11075.
- 18 R. Noyori and T. Ohkuma, *Angew. Chem., Int. Ed.*, 2001, **40**, 40–73.
- 19 (a) X. Yang and M. B. Hall, *J. Am. Chem. Soc.*, 2010, **132**, 120–130; (b) K. S. Sandhya and C. H. Suresh, *Organometallics*, 2011, **30**, 3888–3891; (c) C. Ma, S. Piccinin and S. Fabris, *ACS Catal.*, 2012, **2**, 1500–1506; (d) K. S. Sandhya,



- G. S. Remya and C. H. Suresh, *Inorg. Chem.*, 2015, **54**, 11150–11156.
- 20 In several cases, transition states were calculated to have a lower free energy than a connected intermediate species. In each case, we have verified that the intermediate is lower in energy on the optimized electronic energy surface. See the Computational Methods section for details.
- 21 F. Hasanayn and A. Baroudi, *Organometallics*, 2013, **32**, 2493–2496.
- 22 L. N. Dawe, M. Karimzadeh-Younjali, Z. Dai, E. Khaskin and D. G. Gusev, *J. Am. Chem. Soc.*, 2020, **142**, 19510–19522.
- 23 N. E. Smith, W. H. Bernskoetter and N. Hazari, *J. Am. Chem. Soc.*, 2019, **141**, 17350–17360.
- 24 A. Kumar, N. von Wolff, M. Rauch, Y. Q. Zou, G. Shmul, Y. Ben-David, G. Leitus, L. Avram and D. Milstein, *J. Am. Chem. Soc.*, 2020, **142**, 14267–14275.
- 25 S. Hoops, S. Sahle, R. Gauges, C. Lee, J. Pahle, N. Simus, M. Singhal, L. Xu, P. Mendes and U. Kummer, *Bioinformatics*, 2006, **22**, 3067–3074.
- 26 (a) L. Artús Suárez, Z. Culakova, D. Balcells, W. H. Bernskoetter, O. Eisenstein, K. I. Goldberg, N. Hazari, M. Tilset and A. Nova, *ACS Catal.*, 2018, **8**, 8751–8762; (b) Y. Yu, Y. Zhu, M. N. Bhagat, A. Raghuraman, K. F. Hirsekorn, J. M. Notestein, S. T. Nguyen and L. J. Broadbelt, *ACS Catal.*, 2018, **8**, 11119–11133; (c) M. Jaraíz, J. E. Rubio, L. Enríquez, R. Pinacho, J. L. López-Pérez and A. Lesarri, *ACS Catal.*, 2019, **9**, 4804–4809; (d) J. A. Rogers and B. V. Popp, *Organometallics*, 2019, **38**, 4533–4538; (e) R. Perez-Soto, M. Besora and F. Maseras, *Org. Lett.*, 2020, **22**, 2873–2877; (f) K.-A. Green and J. M. Hoover, *ACS Catal.*, 2019, **10**, 1769–1782.
- 27 E. Brunner, *J. Chem. Eng. Data*, 1985, **30**, 269–273.
- 28 (a) C. B. Kretschmer and R. Wiebe, *J. Am. Chem. Soc.*, 1949, **71**, 1793–1797; (b) J. Guzman, A. Teja and W. Kay, *Fluid Phase Equilib.*, 1981, **7**, 187–195.
- 29 Y. Xu, H. Li, C. Wang, L. Ma and S. Han, *Ind. Eng. Chem. Res.*, 2005, **44**, 408–415.
- 30 (a) S. A. Morris and D. G. Gusev, *Angew. Chem., Int. Ed.*, 2017, **56**, 6228–6231; (b) D. G. Gusev and D. M. Spasyuk, *ACS Catal.*, 2018, **8**, 6851–6861.
- 31 E. Balaraman, B. Gnanaprakasam, L. J. W. Shimon and D. Milstein, *J. Am. Chem. Soc.*, 2010, **132**, 16756–16758.
- 32 C. F. Macrae, P. R. Edgington, P. McCabe, E. Pidcock, G. P. Shields, R. Taylor, M. Towler and J. van de Streek, *J. Appl. Cryst.*, 2006, **39**, 453–457.

